MEASURING RADAR CROSS SECTION OF COMMON SPACECRAFT MATERIALS

Jessica Arnold Headstream[(1)], Alyssa Manis[(2)], Mark Matney[(3)], Michael Magaletta[(4)]

[(1)] *NASA Johnson Space Center, 2101 NASA Pkwy., XI511, Houston, TX 77058, USA, Email: jessica.headstream@nasa.gov*
[(2)] *NASA Johnson Space Center, 2101 NASA Pkwy., XI511, Houston, TX 77058, USA, Email: alyssa.p.manis@nasa.gov*
[(3)] *NASA Johnson Space Center, 2101 NASA Pkwy., XI511, Houston, TX 77058, USA, Email: mark.matney-1@nasa.gov*
[(4)] *Amentum Services, Inc., NASA Johnson Space Center, 2101 NASA Pkwy., XI5-9E, Houston, TX 77058, USA, Email: michael.magaletta123@gmail.com*

ABSTRACT

A fundamental characteristic required to model the orbital debris environment is the size of orbital debris objects, particularly fragmentation debris. The NASA Orbital Debris Program Office (ODPO) receives ground-based radar measurements from both the Haystack Ultrawideband Satellite Imaging Radar (HUSIR) and the Goldstone Orbital Debris Radar System (Goldstone) to characterize the distribution of sub-centimeter debris in low Earth orbit (LEO). Debris size is not directly measured by radar but inferred from the measured radar cross section (RCS). To interpret the observed RCS of orbital debris objects detected by radar measurements as physical sizes, NASA uses an empirical size estimation model (SEM) developed from 1990 to 1991 based on laboratory RCS measurements of breakup fragments generated during hypervelocity impact tests as well as some pieces of "artificial" debris-like objects expected to be representative of the debris population. The ODPO is working to update the NASA SEM based on planned laboratory RCS measurements of debris fragments from DebriSat, a ground-based hypervelocity impact experiment conducted in 2014. The DebriSat target consisted of a high-fidelity, modern engineering model characteristic of a LEO spacecraft.

As a validation step before measuring DebriSat fragments, a set of calibration targets with well-defined geometries and material compositions were measured at The Ohio State University's ElectroScience Laboratory (OSU-ESL) compact radar range. Calibration targets include idealizations of typical shape categories seen in DebriSat fragments, such as nuggets, flat plates, and cylinders. As with DebriSat, calibration target materials were chosen to represent typical modern-day spacecraft components and include stainless steel, aluminum, printed circuit board (PCB) substrate, and carbon fiber reinforced polymer (CFRP). These materials also represent a wide range of electrical conductivities that strongly influence measured RCS and inferred target size. Conductivities of spacecraft materials range from electrically conducting materials, such as stainless steel and aluminum, to non-conducting materials, such as circuit board substrate. The RCS calibration measurements were collected over a frequency sweep from 2 to 18 GHz and stepping through different azimuth angles from 0 to 360 degrees at an elevation of 0 degrees. Results of these laboratory RCS measurements will be presented as charts of azimuthal RCS and RCS versus frequency and will include comparisons with computational models for selected samples. The application of laboratory RCS measurements to orbital debris radar data will also be discussed, particularly comparing the circular polarization behavior of conductive versus dielectric materials. The paper will then outline the next steps for choosing representative DebriSat fragments for laboratory RCS measurements that will contribute to the planned update to the NASA SEM.

1 BACKGROUND

Radar measurements are the primary source of data on orbital debris of a few millimeters to several centimeters in size. Since 1990, the NASA Orbital Debris Program Office (ODPO) has partnered with the U.S. Department of Defense and the Massachusetts Institute of Technology Lincoln Laboratory (MIT/LL) to collect data using the Haystack Ultrawideband Satellite Imaging Radar (HUSIR) and its predecessor, Haystack. Additionally, the Goldstone Orbital Debris Radar System (Goldstone), part of the Deep Space Communications Complex near Barstow, California, and operated by the NASA Jet Propulsion Laboratory, has contributed data to the ODPO since 1993.

An object's size is the primary characteristic of interest for developing models of the orbital debris environment, but size is not directly measured by the radar. Radar cross section (RCS) is the area a hypothetical isotropic scatterer would need to have to account for the reflected power received from a target and is usually expressed in meters squared (m^2) or decibels per meter squared (dBsm). The RCS of a target depends on several factors, including: the true cross-sectional area, size of the object relative to transmit frequency, aspect angle of the object relative to the transmitted beam, material dielectric

Proc. 9th European Conference on Space Debris, Bonn, Germany, 1–4 April 2025, published by the ESA Space Debris Office
Editors: S. Lemmens, T. Flohrer & F. Schmitz, (http://conference.sdo.esoc.esa.int, April 2025)

properties, and material polarization properties. Therefore, inferring absolute target size from RCS is challenging. Furthermore, the relationship between RCS and absolute size is not always one-to-one, particularly if the targets are approximated as spheres, as is often done to reduce the complexity of the problem. This non-unique relationship is demonstrated by the blue line in Fig. 1, which represents RCS versus size expressed as diameter/wavelength for a perfectly conducting sphere. Any given measured RCS may correspond to multiple sizes.

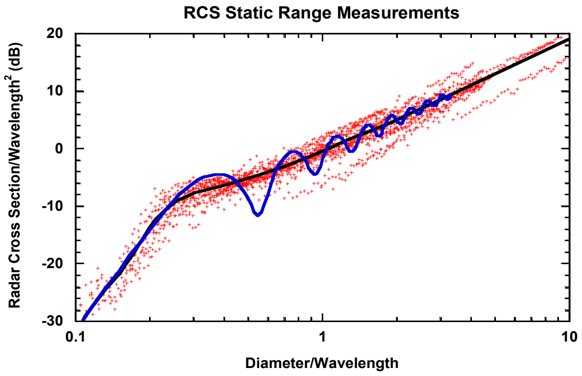

Figure 1. Results of RCS-to-size measurements on 39 representative debris objects (red +). The oscillating blue curve is the RCS for a spherical conductor while the smooth black curve represents the NASA SEM and is the polynomial fit to the data.

To infer debris size from ground-based orbital debris radar measurements, NASA developed its Size Estimation Model (NASA SEM), an empirical one-to-one conversion between RCS and size based on a series of laboratory RCS measurements that accounts for the complexities caused by variations in debris fragment shapes and materials [1, 2, 3]. The NASA SEM is shown in Fig. 1 as the black polynomial fit to the measured fragment data. In the NASA SEM, debris size is characterized by a parameter known as characteristic length (L_c). L_c is defined as the average of the three longest, orthogonal projected dimensions for an object. The RCS measurements upon which the NASA SEM is based were carried out on 39 fragments generated by a series of hypervelocity impact tests on targets made from common spacecraft materials as well as several "artificial debris" fragments not from hypervelocity impact tests [2, 3]. These measurements were conducted in 1990 and 1991, and there have been significant developments in the types of materials used to build spacecraft since then. Such changes in modern spacecraft design were made evident by the unusual size distribution of Iridium 33 fragments compared with other breakup cloud fragments [4, 5]. The ODPO is updating both the NASA SEM and corresponding optical SEM (oSEM) — relating measured optical magnitude to size — to account for these changes in spacecraft design and materials since 1990 and 1991.

To update the NASA SEM and optical SEM (oSEM), an ensemble of fragments from the DebriSat experiment will be statistically selected that best represent the whole of modern spacecraft for RCS and optical characterization. DebriSat consisted of a laboratory hypervelocity experiment conducted in 2014 against a high-fidelity representative model of a modern satellite that was intended to help update NASA and Department of Defense breakup models [6]. Like the SEM, the current NASA Standard Satellite Breakup Model (SSBM) is also primarily based on data from legacy materials. As of February 2025, more than 299,000 fragments visually assessed to have a dimension approximately 2 mm and larger have been collected from the experiment.

To lay the groundwork for interpreting RCS measurements of these fragments, many of which have complex shapes and/or are composed of multiple materials, a set of calibration targets with well-defined geometries and material composition have been chosen to evaluate the capabilities as well as limitations of laboratory radar range measurements. The Ohio State University ElectroScience Laboratory (OSU-ESL) was selected for these measurements due to schedule and capabilities. Additionally, computational electromagnetic (CEM) RCS simulations are being used to compare to the laboratory results.

2 CALIBRATION TARGETS

Because many of the DebriSat fragments have complex shapes and/or are composed of multiple materials, it is necessary to evaluate the capabilities and limitations of the laboratory measurements before selecting fragments for further analysis. A set of calibration targets with well-defined geometries and material compositions were chosen for such an evaluation. Calibration target shapes include spheres, flat plates, and cylinders. As with DebriSat, calibration target materials were chosen to represent typical modern-day spacecraft components and include stainless steel, aluminum, printed circuit board (PCB) substrate, and carbon fiber reinforced polymer (CFRP). These materials also represent a wide range of electrical conductivities, which strongly influences measured RCS and inferred target size. A total of 16 calibration targets were measured, with characteristics listed in Tab. 1. All targets were of solid construction. Hollow targets will be tested in a subsequent round of measurements.

Table 1: Calibration test targets. All targets were of solid construction.

Test #	Shape L_c	Material	Dimensions		
			Diameter	*Length*	*Thickness*
1	Sphere 2.4 cm	SS, polished	2.4 cm	--	--
2	Sphere 1 cm	SS, polished	1 cm	--	--
3	Sphere 6 mm	SS, polished	6 mm	--	--
4	Sphere 3 mm	SS, polished	3 mm	--	--
5	Rod 13.2 mm	SS, polished	3.175 mm	3 cm	--
6	Rod 4.9 mm	SS, ground	1.5875 mm	1 cm	--
7	Square Plate 30.5 mm	Al, polished	--	3 cm x 3 cm	3.175 mm
8	Round Plate 52.8 mm	CFRP, twill	7.62 cm	--	2.921 mm
9	Square Plate 145.6 mm	CFRP, twill	--	15.24 cm x 15.24 cm	2.921 mm
10	Rod 13.2 mm	CFRP, pultruded unidirectional	3.175 mm	3 cm	--
11	Square Plate 29.3 mm	FR4 (PCB)	--	3 cm x 3 cm	1.57 mm
12	Square Plate 289.1 mm	CFRP, unidirectional	--	30.48 cm x 30.48 cm	2.54 mm
13	Square Plate 288.3 mm	CFRP, quasi-unidirectional	--	30.48 cm x 30.48 cm	1.397 mm
14	Round Plate 22.2 mm	Al	3 cm	--	3.175 mm
15	Rod 16.5 mm	CFRP, pultruded unidirectional	3.175 mm	4 cm	--
16	Rod 16.5 mm	Cu	3.175 mm	4 cm	--

The CFRP targets have various weaves and surface textures, including twill, with a glass reflective gloss surface on one side and a matte texture on the reverse; pultruded unidirectional, with a gloss surface on both sides and fibers running in a single direction; and quasi-unidirectional, with a woven texture where bundles of CFRP fibers are held together with plastic "string."

In addition to size and shape, RCS is strongly dependent on the electrical conductivity of the target. Tab. 2 gives a summary of the electrical conductivity of the materials used to fabricate the calibration targets. The electrical conductivity of CFRP is strongly dependent on fiber direction and is much higher along the fiber direction than perpendicular to fiber direction [7]. The conductivity of unidirectional CFRP is lower than that of metals by a factor of about 1,000 along the fiber direction. The conductivity is roughly 100 times lower perpendicular to the fiber direction than along the fiber direction [7]. FR4 is a substrate for circuit boards and is therefore designed to be a very efficient electrical and thermal insulator.

Table 2: Material conductivities of calibration target materials at room temperature. Conductivity is given in siemens per meter [S/m].

Material	**Electrical Conductivity [S/m]**
Copper	57.60 x 10^{6}[*]
Aluminum	21.11 x 10^{6}[*]
Stainless-steel	1.77 x 10^{6}[*]
CFRP	~10^{2} to 10^{4}[6]
FR4	Electrical insulator

*Source: *Janzic, M. (2004) NIST Technical Note 1531, DC Conductivity Measurements of Metals, p 11 first column of Table 3.*

3 THE OSU-ESL RADAR RANGE

Calibration measurements were conducted in the OSU-ESL compact radar range. Within the radar range, samples are mounted on a large, motorized rotator that can rotate a full 360° in azimuth. The facility, including foam test positioner, is shown in Fig. 2. The OSU-ESL can measure frequencies from 2 to 18 GHz with a single setup and can cover 1 to 2 GHz with a second setup. The radar range calibration targets were measured with the 2 to 18 GHz configuration. A frequency sweep with 10 MHz resolution was conducted at each azimuth angle over a range of predefined azimuth angles as the foam positioner was rotated. A full set of linear polarization measurements, HH, HV, VH, and VV polarizations, were collected for each azimuth/frequency sweep, where H represents horizontal polarization, and V represents vertical polarization. The first letter in the sequence designates the transmitter polarization, and the second letter designates the receiver polarization.

Figure 2. OSU-ESL radar range with the rotating foam test positioner in the center of the image.

For each calibration object, RCS measurements were collected over a full 360° in azimuth. Sphere measurements (Test Nos. 1-4) were collected in 5ºazimuth increments. All other calibration object measurements (Test Nos. 5-16) were collected in 1ºazimuth increments. The larger step size for the spheres was chosen because their RCS is constant with azimuth, allowing more time to be spent on the other targets. Due to the rotational symmetry of the calibration targets, the measurements in azimuth were conducted at a single elevation of 0 degrees. Securing the samples during azimuth rotation required custom low dielectric constant, low-loss target holders. A set of such holders were fabricated from structural foam for the calibration target RCS measurements, as shown in the example in Fig. 3.

Before collecting calibration test target measurements, the radar range was baselined using 12-inch and 6-inch hollow aluminum reference spheres. For each calibration test target a background measurement was collected with the foam test positioner and foam sample holder configuration over the same set of azimuth angles as the actual measurement. A measurement of the foam test positioner over 360 azimuth angles was also collected at least once per day.

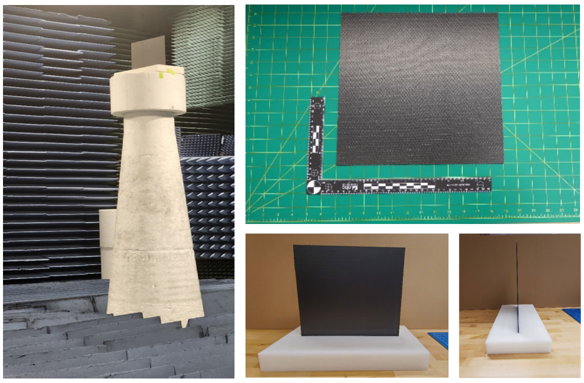

Figure 3. Top right: example of one of the calibration targets, a CFRP square plate. Bottom right: two views of the same target in a custom-made low-loss foam sample holder. Left: target and holder placed on rotating foam positioner pedestal in the OSU-ESL radar range.

4 RESULTS AND DISCUSSION

4.1 Detectability of Small Debris in the OSU-ESL Radar Range

Historically, orbital debris radar data received by the ODPO from HUSIR is complete down to roughly 6 mm at 1000 km altitude, while data received from Goldstone is complete down to 3 mm at 1000 km altitude [8, 9]. One goal of these RCS calibration measurements was to determine whether the signal-to-noise of laboratory RCS measurements is large enough to measure such millimeter-sized objects.

Two small spherical targets, 6 mm (Test 3) and 3 mm (Test 4) in diameter, were used to test the frequency-dependent signal to noise. In theory, the HH and VV polarizations for a sphere should be identical in frequency response and azimuthally independent at each frequency. To support the evaluation of RCS laboratory measurement capabilities and limitations, CEM software was used to verify the initial laboratory calibration dataset. Such software can compute the RCS of homogeneous, high-conductivity targets with arbitrary non-spherical shapes.

The lower panel of Fig. 4 shows the laboratory monostatic RCS as a function of frequency at 0 degrees azimuth for the 6 mm stainless steel sphere (Test 3) at each polarization compared with a computational electromagnetic (CEM) simulation. The measured HH and VV polarizations as a function of frequency overlap as expected and show good agreement with the CEM simulation at frequencies greater than 10 GHz but are noisy below this frequency. The HH and VV signals from the 3 mm sphere (Test 4) reached this noise threshold at an even higher frequency, roughly 15 GHz.

The upper panel of Fig. 4 shows an azimuth cut of the 6 mm spherical target monostatic RCS measurement data at 15 GHz frequency where the HH and VV polarization signal-to-noise is sufficient for detection. At 15 GHz, the HH and VV polarization RCS are nearly identical and independent of azimuth angle, as expected.

The VH and HV polarizations at 15 GHz have a reported RCS of -60 to -50 dBsm, whereas for a perfect sphere these should be close to 0 degrees. This likely represents the noise floor of the measurements and should be kept in mind when interpreting the laboratory measurements. Similarly, below roughly 10 GHz the modeled HH and VV azimuthal responses are also below this noise threshold.

Therefore, as expected, the detectability of small targets is frequency-dependent. HUSIR and Goldstone transmit at frequencies of 10.1 GHz and 8.56 GHz, respectively. At 10 GHz, close to the transmit frequencies of HUSIR and Goldstone, the minimum measurable size in the laboratory is roughly 6 mm, close to the completeness size of HUSIR, but larger than the completeness size of Goldstone.

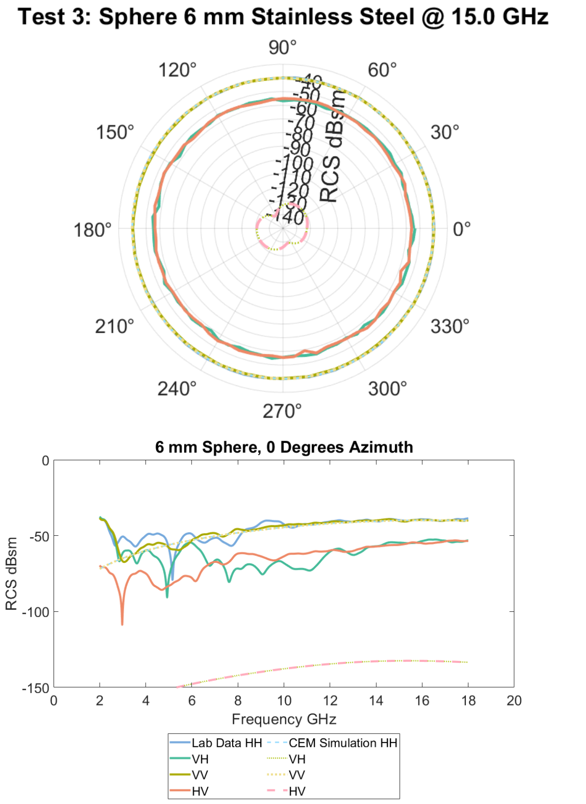

Figure 4. Azimuthal RCS of Test 3, a 6 mm sphere, at 15 GHz (top) and frequency dependant RCS of the same at 0 degrees azimuth (bottom). Lab data for each polarization are denoted by the solid lines, while CEM simulations are shown as dashed lines.

4.2 Influence of Target Shape, Size, and Layup on RCS Versus Azimuth Angle

Target geometry – including shape, size, and texture – influences the measured RCS as this determines the geometric cross section of an object at a given aspect angle. The RCS calibration targets were selected so that comparisons of each of these factors could be assessed. The influence of shape was considered by comparing targets according to the L_c parameter discussed in Section 1. Size was compared using RCS measurements of two rods with the same material composition and radius, but different lengths. Texture was assessed by comparing the RCS of two CFRP plates with different carbon fiber layups.

Fig. 5 shows the azimuthally dependent HH and VV RCS at 10 GHz for two highly conducting objects, one spherical and another non-spherical, with similar L_c, 24 mm for the sphere versus 22.2 mm for the plate. While the sphere is stainless steel and the plate is aluminium, the conductivity of both of these is high enough that it should not appreciably affect the measure RCS. At 0 degrees incidence, the plate was oriented with the broad side directly perpendicular to the incident beam. As expected, the sphere does not vary in RCS with aspect angle, with minor variations likely due to the sphere placement being slightly off-center from the center of the foam positioner. In contrast, the plate shows a higher RCS when the beam is incident on the broad side (0 degrees and 180 degrees) than near the edges (90 degrees and 270 degrees).

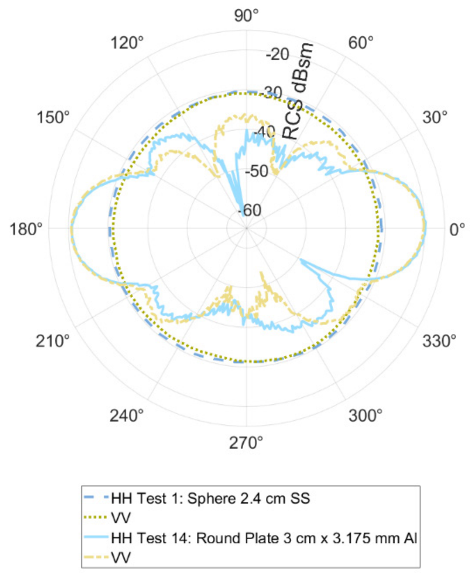

Figure 5. Comparison of Test 1, the 2.4 cm sphere, and Test 14, the 3 cm diameter round plate, at 10 GHz. Both objects have a similar L_c, 24 mm for the sphere versus 22.2 mm for the plate. This figure demonstrates the very different azimuthally dependent monostatic RCS between the spherical versus non-spherical object.

Fig. 6 shows the azimuthally dependent HH and VV RCS at 10 GHz of two CFRP rods with the same radius and different lengths. Both rods were oriented such that the length of the rod was parallel to the foam platform as the platform rotated. The lengths of the rods were also perpendicular to the incoming beam at 0 degrees incidence. As expected, the RCS is higher for the longer versus the shorter rod in both the HH (solid blue line versus blue dashed line) and VV (dashed yellow line versus dotted dark yellow line) for polarizations near 0 degrees and 180 degrees (beam incident perpendicular to the length of the rod). In addition, for both rods, the HH and VV RCS is highest when the length of the rod is facing the transmitted beam (0 degrees and 180 degrees) because the cross-sectional area of the length of the rod is much larger than that of each end. The RCS drops to the noise floor when the end of the rod is facing the transmitted beam (90 degrees and 270 degrees).

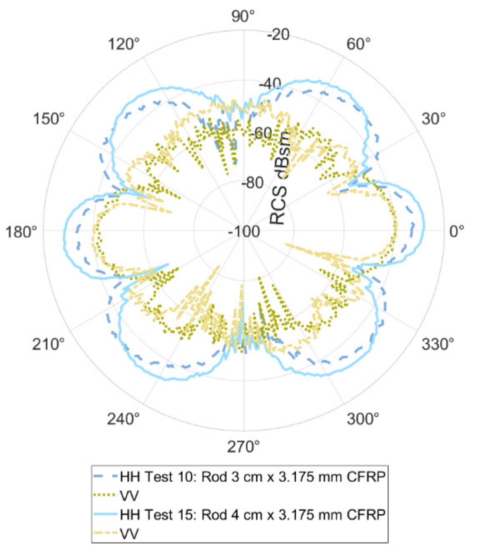

Figure 6. Comparison of two CFRP rods, Test 10 and Test 15, at 10 GHz. The two rods have the same radius, but the Test 15 rod is longer. At 0 degrees and 180 degrees, the RCS of the longer rod is higher in both the HH and VV polarizations.

Fig. 7 compares two large, 30-cm-x-30-cm, CFRP plates with two different layups of the carbon fiber strands, one with a unidirectional weave (Test 12) and the other with a quasi-unidirectioal weave (Test 13). Both plates were oriented so that the broad, square face was perpendicular to the incoming beam at 0 degrees azimuth. The unidirectional components of the weaves were oriented parallel to the surface of the rotating foam stage.

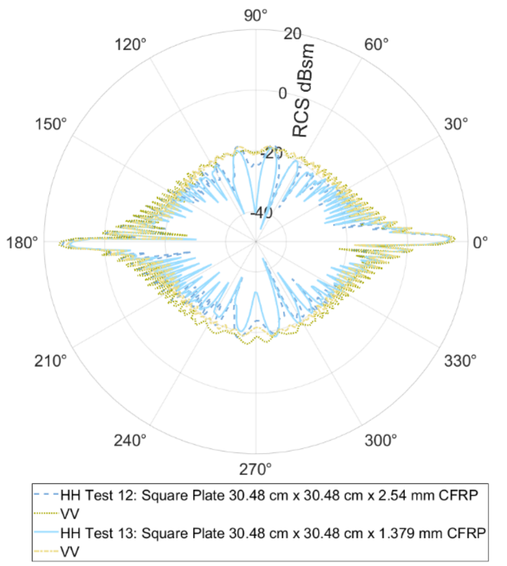

Figure 7. Comparison of two CFRP plates, Test 12, CFRP plate with a unidirectional weave and Test 13, CFRP plate with a quasi-unidirectional weave, both at 10 GHz. The two plates are square with 30.48 cm sides, and the square face of the plates were perpendicular to the incoming beam at 0 degrees azimuth.

The unidirectional plate had a glossy surface on both sides while the quasi-unidirectional plate had a matte surface on one side and a glossy surface on the other. The matte surface was placed facing the incident beam at 0 degrees azimuth. Both plates show a fringe pattern in RCS azimuth, likely due to the woven structure of the embedded carbon fiber strands. The effects of the weave directions are subtle but discernible in the HH linear polarization results. Away from 0 degrees and 180 degrees, the quasi-unidirectional weave (Test 13) has a much larger contrast in RCS than the unidirectional weave (Test 12). The VV linear polarization component is similar in magnitude between both plates from 0 degrees, through 90 degrees to 180 degrees, but slightly different from 180 degrees, through 270 degrees, to 0 degrees.

4.3 Material Conductivity

Also of interest is the difference in RCS between objects of the same shape and size but made of materials with very different dielectric constants. Fig. 8 shows the change in RCS with azimuth for two different rods (Test 15 and Test 16), where one rod is made from CFRP while the other is made from copper. Both rods have the exact same dimensions and were oriented such that the length of the rod was parallel to the foam platform as the platform rotated. The lengths of the rods were also perpendicular to the incoming beam at 0 degrees incidence. Both materials have a very similar RCS response, despite the large difference in dielectric constant. This demonstrates that CFRP behaves much like a conductor. This could be due to the layup of the CFRP fibers, for example if fibers lay in the direction of the length of the rod, leading to the CFRP rod showing behavior similar to the copper conductor.

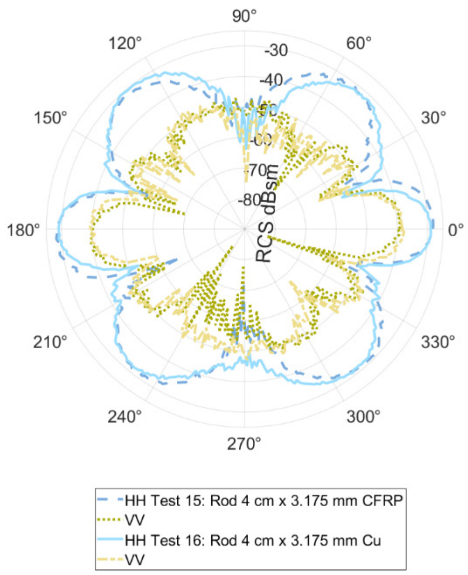

Figure 8. Comparison of Test 15, CFRP rod, and Test 16, copper rod, at 10 GHz. These two rods have the exact same dimensions. The two materials show a similar azimuthally dependent RCS, with some differences in the HH polarization.

4.4 Comparison with Computational Electromagnetic Simulation

DebriSat fragment selection will need to account for laboratory instrumental limitations, such as the minimum detectable size of various materials, as was discussed in Section 4.1. For example, the limiting size at 10 GHz was found to be ~ 6 mm for OSU-ESL radar measurements, but smaller sizes can be assessed using simulation models, such as CEM software. Fig. 9 shows a comparison between the measured RCS and software simulated RCS for one of the calibration targets, a copper rod (Test 16), where the transmitted electromagnetic (EM) beam is perpendicular to the length of the rod at 0 degrees. Fig. 9 demonstrates good agreement between the laboratory measurements and model for the HH polarization configuration, while the simulated VV signal agrees well between the two models but is near or below the noise floor of the lab measurements at angles far from 0 degrees and 180 degrees. This is because the cross-sectional area of the length of the rod is much larger than that of each end.

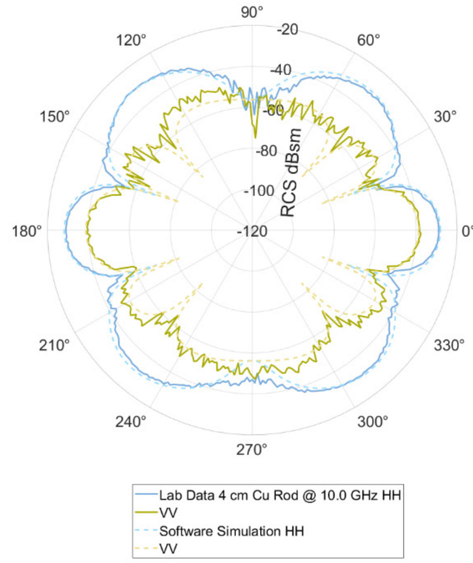

Figure 9. Comparison of Test 16, a copper rod, between the laboratory measurements and CEM simulation at 10 GHz. There is good agreement between the laboratory measurements and the CEM simulations where the laboratory measurements have high signal-to-noise.

CEM models can also be used to examine the properties of polarizing materials. Fig. 10 demonstrates that a woven CFRP plate polarizes the returned signal, leading to a non-negligible cross-polar (HV) return, while a perfectly conducting target of the same shape and size would return the same linear polarization, resulting in very small cross-polar (HV, VH) returns. This may be due to the construction of CFRP, which is woven from carbon fiber strands embedded in polymer. Depending on the layup, the carbon fiber strands can be unidirectional, bidirectional, or quasi-unidirectional, altering the polarization from that of a perfect conductor.

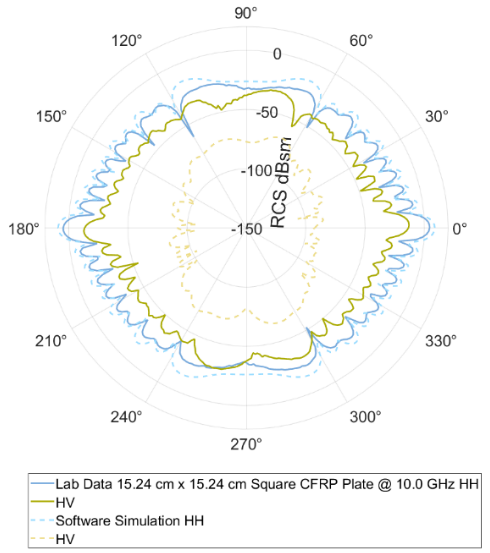

Figure 10. Comparison of Test 9, a CFRP plate, between the laboratory measurements and CEM simulation of a perfect conductor at 10 GHz. There is good agreement between the laboratory measurements and the CEM simulations for the HH polarization, although the lab data has a slightly smaller RCS at all azimuth angles than the simulated data. There is substantial disagreement for the HV polarization, as the perfectly conducting simulation does not capture the polarizing properties of the CFRP.

4.5 4.5 Conversion to Circular Polarization

Both HUSIR and Goldstone transmit and receive circularly polarized signals. Therefore, to apply the linearly polarized laboratory RCS data to understand the orbital debris data collected by these instruments, it is necessary to convert the results to circular polarization. Given the full linear polarization scattering matrix in HH, VV, HV, and VH the full circular polarization scattering matric can be synthesized. To calibrate the laboratory RCS data and confirm the linear-to-circular polarization conversion, RCS data of the 2.4 cm stainless steel sphere measured in Test 1 were compared with the ideal computed values. We then used this calibration to perform the same conversion for other targets.

Of particular interest is the difference in circular polarization properties of targets with the same shape but made of materials with dissimilar conductivities. Fig. 11 compares the circularly polarized RCS versus azimuth of a CFRP rod (Test 15) versus a copper rod (Test 16) at 10 GHz for both the principal polarization (PP), top left, and orthogonal polarization (OP), top right, as well as the circular polarization (CP) ratio, bottom. Both rods have similar RCS in both the PP and OP polarizations, as would be expected for dipoles. As before, this may be due to the layup of the CFRP rod, leading to behavior similar to that of the conducting copper rod.

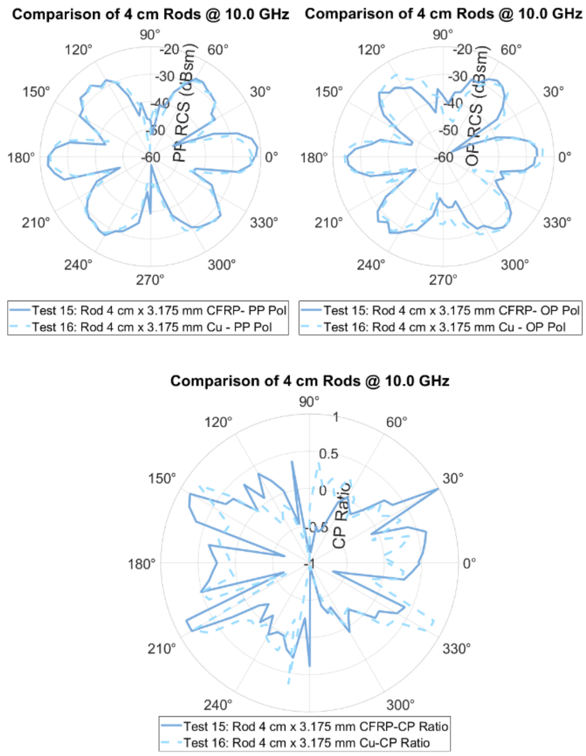

Figure 11. Comparison of circular polarization properties for Test 15, a CFRP rod, and Test 16, a copper rod, at 10 GHz. These two rods have the exact same dimensions. Top left shows the PP polarization, top right shows the OP polarization, and the bottom shows the CP ratio. The two materials show a similar azimuthally dependent RCS in both PP and OP.

As with the linearly polarized RCS measurements, it is worth understanding the difference between objects of similar conductivity and L_c, but different shape, in circular polarization. Fig. 12 shows the azimuthally dependant circular PP RCS for the same objects compared in Fig. 5: Test 1, a 2.4 cm stainless steel sphere with $L_c = 24$ mm, and Test 14, a 3 cm diameter circular aluminum plate with $L_c = 22.2$ mm. Despite having a similar effective diameter in terms of L_c, the PP RCS of the plate differs substantially from a sphere depending on the azimuthal aspect angle.

The purpose of orbital debris radar data, however, is to provide a statistical sampling of debris clouds. Assuming that any given debris shape category and size will be observed multiple times at random orientations, the NASA SEM should give an accurate size estimate over this population. Fig. 13 shows the total RCS of the same two objects, Tests 1 and 14, as well as the azimuthally averaged total RCS of Test 14, the circular plate. Despite the 3 cm aluminum plate having a slightly smaller L_c and lower conductivity than the stainless steel sphere, the azimuthally averaged total RCS of the $L_c = 22.2$ mm plate is higher than the $L_c = 24$ mm sphere by about 3 dBsm.

It should be noted, however, that low signal-to-noise in the lab data at some aspect angles, particularly the plate edges, may affect this averaged RCS value.

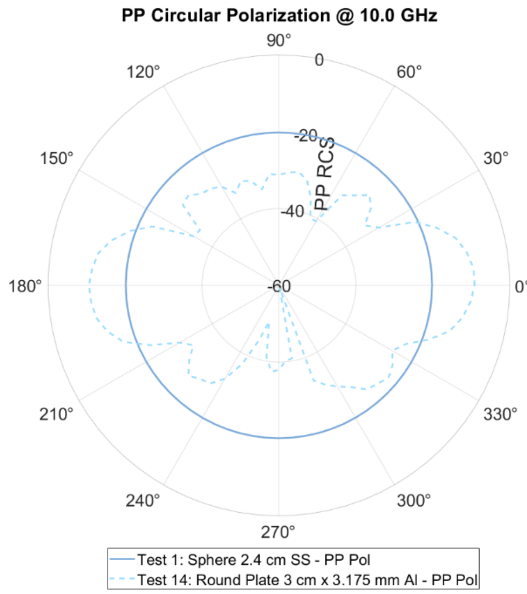

Figure 12. Comparison of the PP RCS (dBsm) for Test 1, a stainless steel sphere, and Test 14, a round aluminum plate, at 10 GHz. These objects have L_c = 24 mm and L_c = 22.2 mm, respectively.

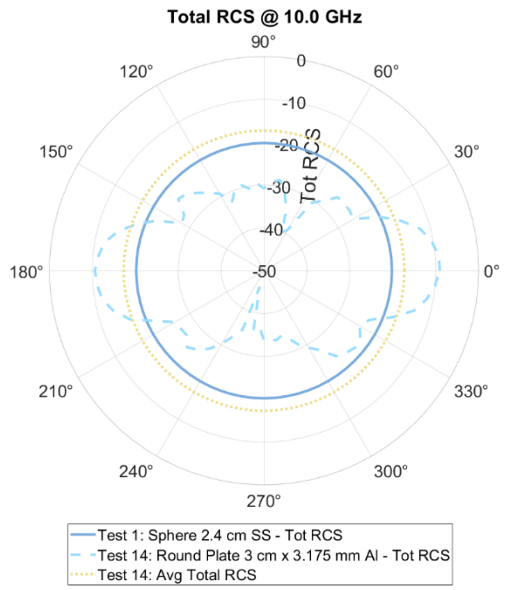

Figure 13. Comparison of the total RCS (dBsm) for Test 1, a stainless steel sphere, and Test 14, a round aluminum plate, at 10 GHz. These objects have L_c = 24 mm and L_c = 22.2 mm, respectively. Also shown is the azimuthally averaged total RCS for Test 14.

5 CONCLUSIONS

A set of laboratory RCS calibration measurements were analyzed covering a variety of materials and shapes representative of modern-day spacecraft, as used in the DebriSat project. These measurements demonstrate the feasibility and limitations of using a radar range facility to collect RCS measurements of calibration targets with sizes and materials compositions representative of OD, but simplified, well characterized shapes. The influence of size, shape, and material conductivity on the measured RCS over both frequency and azimuth was examined. Measurements were also compared to CEM models of the calibration targets. Notable results from these calibration test target measurements include:

1) The limiting size for the OSU-ESL radar range RCS measurements was about 6 mm at 10 GHz, the relevant frequency for comparisons with HUSIR orbital debris measurements.
2) Despite the conductivity of CFRP being several orders of magnitude lower than copper, the unidirectional CFRP rod of the same size had a similar RCS to copper.
3) Woven CFRP plates have large cross-polar terms that require the incorporation of a dielectric tensor for accurate CEM models, rather than using a single value.
4) As expected, target shape has a large effect on the RCS observed at any given aspect angle for objects with a similar L_c.
5) For one of the test plates when looking at the azimuthally averaged total RCS, representative of a debris population at random orientations, the averaged total RCS was close to that of an equivalent sphere.

The results of this study using simple calibration shapes show good agreement with CEM analysis and provides the foundation for the next step of measuring calibration targets that include more complex shapes and multi-material samples. Subsequent radar range RCS measurements will focus on evaluating possible sample holder materials with higher durability than the low-loss foam used for the calibration measurements and measuring additional calibration targets with more complex shapes, such as bent plates or rods as well as mixed materials in preparation for the more complex DebriSat fragment shapes. Additionally, a subset of calibration targets will be assessed in the ODPO's Optical Measurements Center (OMC) and compared to the laboratory RCS measurements to help bridge the radar and optical SEMs.

This next phase of calibration measurements will further inform the methodology necessary to successfully collect RCS measurements of actual DebriSat fragments.

6 REFERENCES

1. Xu, Y. L., Stokely, C., Matney, M., & Stansbery, E. (2005). A Statistical Size Estimation Model for Haystack and HAX Radar Detections. *Proc. 56th International Astronautical Congress*, Fukuoka, Japan, IAC-05-B6.1.02.

2. Bohannon, G., Dalquist, C., & Pardee, M. (1991). Physical Descriptions of Debris Objects Used in Static RCS Measurements. XonTech Report 910555-1978.

3. NASA ODPO (2008). Handbook for Limiting Orbital Debris. NASA-Handbook 8719.14.

4. Liou, J.-C. (2009). An Update on Recent Major Breakup Fragments, *NASA Orbital Debris Quarterly News*, **13**(3), 5-6.

5. Garrison, T.P., Ince, M., Pizzicaroli, J., et al. (1997). System engineering trades for the Iridium constellation, *J. Spacecraft & Rockets,* **34**(5), 675-680.

6. Liou, J.-C., Opiela, J., Cowardin, H., et al. (2014). Successful Hypervelocity Impacts of DebrisLV and DebriSat, *NASA Orbital Debris Quarterly News* **18**(3), pp. 3-5.

7. Zhao, Q., et al. (2019). Review on the Electrical Resistance/Conductivity of Carbon Fiber Reinforced Polymer, *Applied Sciences*, **9**(11), 2309.

8. Murray, J. & Matney, M. (2023). Haystack Ultrawideband Satellite Imaging Radar Measurements of the Orbital Debris Environment: 2021, NASA/TP-20230008344.

9. Arnold, J. A., Murray, J., Murray, M., Matney, M. & Kennedy, T. (2024). Goldstone Radar Measurements of the Orbital Debris Environment: 2020-2021, NASA/TP-20240002199.